

ON THE ROLE OF DISKS IN THE FORMATION OF STELLAR SYSTEMS: A NUMERICAL PARAMETER STUDY OF RAPID ACCRETION

KAITLIN M. KRATTER¹, CHRISTOPHER D. MATZNER¹, MARK R. KRUMHOLZ², AND RICHARD I. KLEIN^{3,4}

¹ Department of Astronomy and Astrophysics, 50 St. George Street, University of Toronto, Toronto, Ontario M5R 3H4, Canada

² Department of Astronomy, 201 Interdisciplinary Sciences Building, University of California, Santa Cruz, CA 95064, USA

³ Department of Astronomy, University of California, Berkeley 601 Campbell Hall, Berkeley, CA 94720-3411, USA

⁴ Lawrence Livermore National Laboratory, AX Division 7000 East Avenue, Livermore, CA 94550, USA

Received 2009 July 15; accepted 2009 November 19; published 2009 December 23

ABSTRACT

We study rapidly accreting, gravitationally unstable disks with a series of idealized global, numerical experiments using the code ORION. Our numerical parameter study focuses on protostellar disks, showing that one can predict disk behavior and the multiplicity of the accreting star system as a function of two dimensionless parameters which compare the infall rate to the disk sound speed and orbital period. Although gravitational instabilities become strong, we find that fragmentation into binary or multiple systems occurs only when material falls in several times more rapidly than the canonical isothermal limit. The disk-to-star accretion rate is proportional to the infall rate and governed by gravitational torques generated by low- m spiral modes. We also confirm the existence of a maximum stable disk mass: disks that exceed $\sim 50\%$ of the total system mass are subject to fragmentation and the subsequent formation of binary companions.

Key words: accretion, accretion disks – binaries: general – stars: formation – stars: low-mass, brown dwarfs

Online-only material: color figures

1. INTRODUCTION

During the earliest phases of star formation, protostellar disks are deeply embedded within their natal clouds. Observing this stage has been difficult because the source is only visible at wavelengths where resolution is poor. But because it sets the initial conditions for stellar and planetary systems, an understanding of this phase is critical. Models of rapidly accreting disks are thus vital for the interpretation of observations of future facilities such as ALMA and the EVLA.

In this paper, we focus on the dynamics of disks around young, rapidly accreting protostars, for which self-gravity is the key ingredient (Lin & Pringle 1987; Gammie 2001; Kratter et al. 2008). Gravitational instability (GI) is important whenever disks are cold enough or massive enough to trigger it, as they typically are during the early phases of star formation. GI plays a strong role in active galactic nucleus (AGN) disks as well, and possibly in other contexts where disks are cold and accretion is fast.

The role of GI in angular momentum transport is complicated by the fact that it can lead to runaway collapse. Indeed, this makes GI an attractive mechanism for the formation of stars with companions (binaries and brown dwarfs; Bonnell & Bate 1994a, 1994b; Whitworth et al. 2007). Kratter & Matzner (2006, hereafter KM06) and Kratter et al. (2008, hereafter KMK08) found that disk fragmentation and binary formation are increasingly likely as one considers more and more massive stars, whereas disks in low-mass star formation are relatively stable (Matzner & Levin 2005).

Although semi-analytical and low-dimensional studies can illuminate trends and provide useful approximate results, disk fragmentation is inherently a nonlinear and multidimensional process. For this reason we have embarked on a survey of idealized, three-dimensional, numerical experiments to examine the role of GI as the mediator of the accretion rate in

self-gravitating disks, and as a mechanism for creating disk-born companions.

We emphasize that these are numerical experiments, not simulations of star formation. Our goal in conducting experiments is to isolate the important physical process, GI, which dictates angular momentum transport and fragmentation. To do so, we separate the dynamical problem from the thermal one. We exclude thermal physics from our simulations entirely, while scanning a thermal parameter in our survey.

By these means we reduce the physical problem to two dimensionless parameters: one for the disk's temperature and another for its rotation period—both in units determined by its mass accretion rate. We hold these fixed in each simulation by choosing well-controlled initial conditions corresponding to self-similar core collapse. This parameterization is a central aspect of our work: it forms the basis for our numerical survey; it allows us to treat astrophysically relevant disks, including fragmentation and the formation of binary companions, while also maintaining generality; and it distinguishes our work from previous numerical studies of core collapse, disk formation, GI, and fragmentation. We demonstrate that idealized disks like those presented here can capture many of the important features of simulations with more complicated physics, with significantly lower computational cost.

This paper, the first in a series, focuses on the broad conclusions we can draw from our parameter space study; subsequent papers will discuss the detailed behavior of multiple systems, and three-dimensional effects such as turbulence, and vertical flows. We begin here by introducing our dimensionless parameters in Section 2. We describe the initial conditions and the numerical code used in Section 3. In Section 4, we derive analytic predictions for the behavior of disks as a function of our parameters. We describe the main results from our numerical experiments in Section 5, with more detailed analysis in Section 6. We compare them

to other numerical and analytic models of star formation in Section 7.

2. A NEW PARAMETER SPACE FOR STUDYING ACCRETION

We consider the gravitational collapse of a rotating, quasi-spherical gas core onto a central pointlike object, mediated by a disk. In the idealized picture we will explore in this paper, the disk and the mass flows into and out of it can be characterized by a few simple parameters. At any given time, the central point mass (or masses, in cases where fragmentation occurs) has mass M_* , the disk has mass M_d , and the combined mass of the two is M_{*d} . The disk is characterized by a constant sound speed $c_{s,d}$. Material from the core falls onto the disk with a mass accretion rate \dot{M}_{in} , and this material carries mean specific angular momentum $\langle j \rangle_{\text{in}}$, and as a result it circularizes and goes into Keplerian rotation at some radius $R_{k,\text{in}}$; the angular velocity of the orbit is $\Omega_{k,\text{in}}$.

Note that \dot{M}_{in} , j_{in} , $R_{k,\text{in}}$, and $\Omega_{k,\text{in}}$ characterize the material that is just reaching the disk at a given instant, and as a result they can vary with time—indeed, we will set up our initial conditions to guarantee that they do vary with time in precisely the manner required to ensure that certain dimensionless numbers remain constant as gas accretes. In general in what follows, we refer to quantities associated with the central object with subscript “*”, quantities associated with the disk with a subscript “d”, quantities associated with infall with subscript “in”. Angle brackets indicate mass-weighted averages over the disk (with subscript “d”) or over infalling mass (with subscript “in”).

We characterize our numerical experiments using two dimensionless parameters which are well adapted to systems undergoing rapid accretion. Because the behavior of young protostellar disks will be dominated by infall, modeling their behavior in terms of dimensionless accretion rates is a natural choice.

We encapsulate the complicated physics of heating and cooling through the thermal parameter

$$\xi = \frac{\dot{M}_{\text{in}} G}{c_{s,d}^3}, \quad (1)$$

which relates the infall mass accretion rate \dot{M}_{in} to the characteristic sound speed $c_{s,d}$ of the disk material. Our parameter ξ is also related to the physics of core collapse leading to star formation. If the initial core is characterized by a signal speed $c_{\text{eff},c}$ then $\dot{M}_{\text{in}} \sim c_{\text{eff},c}^3 / G$, implying $\xi \sim c_{\text{eff},c}^3 / c_{s,d}^3$ —although there can be large variations around this value (Larson 1972; Foster & Chevalier 1993). The second, rotational parameter

$$\Gamma = \frac{\dot{M}_{\text{in}}}{M_{*d} \Omega_{k,\text{in}}} = \frac{\dot{M}_{\text{in}} \langle j \rangle_{\text{in}}^3}{G^2 M_{*d}^3} \quad (2)$$

compares the system’s accretion timescale, $M_{*d} / \dot{M}_{\text{in}}$ to the orbital timescale of infalling gas. For the initial conditions we use in this work, the quantities $\langle j \rangle_{\text{in}}$ and M_{*d} evolve in time while \dot{M}_{in} remains constant. They can be evaluated as functions of time, or the current radius from which material is falling onto the system. To hold Γ fixed, we specify a core rotation profile such that $\langle j \rangle_{\text{in}} \propto M_{*d}$. Unlike ξ , Γ is independent of disk heating and cooling, depending only on the core structure and velocity field. In general, Γ compares the relative strength of rotation and gravity in the core. Systems with a large value of Γ (e.g., accretion-induced collapse of a white dwarf) gain a significant

amount of mass in each orbit, and tend to be surrounded by thick, massive accretion disks, while those with very low Γ (e.g., AGN) grow over many disk lifetimes, and tend to harbor thin disks with little mass relative to the central object. We consider characteristic values for our parameters in Section 2.1, and their evolution in the isothermal collapse of a rigidly rotating Bonnor–Ebert sphere in Section 7.1.

The parameters ξ and Γ are more flexible than other dimensionless parameters used to characterize collapsing cores such as $\alpha_{\text{therm}} = E_{\text{therm}} / E_{\text{grav}}$ and $\beta_{\text{rot}} = E_{\text{rot}} / E_{\text{grav}}$ (Bodenheimer et al. 1980; Miyama et al. 1984). While the latter rely implicitly on a quasi-static core model, ξ and Γ can be evaluated for arbitrary infall models, and therefore for a wider range of astrophysical disk scenarios. Whereas α_{therm} and β_{rot} are zero-dimensional descriptions of the collapse problem, ξ and Γ can be functions of mass and hence describe time (or scale) evolution.

In order to model disk behavior in terms of these two parameters, we hold ξ and Γ fixed for each experiment via the self-similar collapse of a rotating, isothermal sphere (Section 3.2). This strategy allows us to map directly between the input parameters and relevant properties of the system. Specifically, we expect dimensionless properties such as the disk-to-star mass ratio, Toomre parameter, $Q = c_s \Omega / (\pi G \Sigma)$ (Toomre 1964), stellar multiplicity, etc., to fluctuate around well-defined mean values (see Section 3.4).

We aim to use our parameters ξ and Γ to (1) explore the parameter space relevant to a range of star formation scenarios; (2) better understand the disk parameters, both locally and globally, which dictate the disk accretion rate and fragmentation properties; (3) make predictions for disk behavior based on larger scale, observable quantities; and (4) allow the results of more complicated and computationally expensive simulations to be extended into other regimes.

2.1. Characteristic Values of the Accretion Parameters

We base our estimates of Γ and ξ on observations of core rotation in low-mass and massive star-forming regions (Myers & Fuller 1992; Goodman et al. 1993; Williams & Myers 1999), as well as the analytical estimates of core rotation and disk temperature in Matzner & Levin (2005), Krumholz (2006), KM06, and KMK08. Using simple models of core collapse in which angular momentum is conserved in the collapse process and part of the matter is cast away by protostellar outflows (Matzner & McKee 2000), we find that both ξ and Γ are higher in massive star formation than in low-mass star formation. In our models, the characteristic value of Γ rises from ~ 0.001 to 0.03 as one considers increasingly massive cores for which turbulence is a larger fraction of the initial support.

The value of ξ is more complicated, as it reflects the disk’s thermal state as well as infalling accretion rate, but the models of KMK08 and Krumholz (2006) indicate that its characteristic value increases from < 1 to ~ 10 as one considers higher and higher mass cores—although the specific epoch in the core’s accretion history is also important. In the case of massive stars, such rapid accretion has been observed (Beltrán et al. 2006 and Barnes et al. 2008). Numerical simulations also find rapid accretion rates from cores to disks. Simulations such as those of Banerjee & Pudritz (2007) report $\xi \sim 10$ at early times in both magnetized and non-magnetized models. We note that Γ has significant fluctuations from core to core when turbulence is the source of rotation, and both ξ and Γ are affected by variations of the core accretion rate around its characteristic value (Foster & Chevalier 1993).

3. NUMERICAL METHODOLOGY

3.1. Numerical Code

We use the code ORION (Truelove et al. 1998; Klein 1999; Fisher 2002) to conduct our numerical experiments. ORION is a parallel adaptive mesh refinement (AMR), multi-fluid, radiation-hydrodynamics code with self-gravity and Lagrangian sink particles (Krumholz et al. 2004). Radiation transport and multi-fluids are not used in the present study. The gravito-hydrodynamic equations are solved using a conservative, Godunov scheme, which is second-order accurate in both space and time. The gravito-hydrodynamic equations are

$$\frac{\partial}{\partial t} \rho = -\nabla \cdot (\rho \mathbf{v}) - \sum_i \dot{M}_i W(\mathbf{x} - \mathbf{x}_i), \quad (3)$$

$$\begin{aligned} \frac{\partial}{\partial t} (\rho \mathbf{v}) = & -\nabla \cdot (\rho \mathbf{v} \mathbf{v}) - \nabla P - \rho \nabla \phi \\ & - \sum_i \dot{\mathbf{p}}_i W(\mathbf{x} - \mathbf{x}_i), \end{aligned} \quad (4)$$

$$\begin{aligned} \frac{\partial}{\partial t} (\rho e) = & -\nabla \cdot [(\rho e + P) \mathbf{v}] + \rho \mathbf{v} \cdot \nabla \phi \\ & - \sum_i \dot{\mathcal{E}}_i W(\mathbf{x} - \mathbf{x}_i). \end{aligned} \quad (5)$$

Equations (3)–(6) are the equations of mass, momentum, and energy conservation, respectively. In the equations above, \dot{M}_i , $\dot{\mathbf{p}}_i$, and $\dot{\mathcal{E}}_i$ describe the rate at which mass and momentum are transferred from the gas onto the i th Lagrangian sink particles. Summations in these equations are over all sink particles present in the calculation. $W(\mathbf{x})$ is a weighting function that defines the spatial region over which the particles interact with gas. The corresponding evolution equations for sink particles are

$$\frac{d}{dt} M = \dot{M}_i, \quad (6)$$

$$\frac{d}{dt} \mathbf{x}_i = \frac{\mathbf{p}_i}{M_i}, \quad (7)$$

$$\frac{d}{dt} \mathbf{p}_i = -M_i \nabla \phi + \dot{\mathbf{p}}_i. \quad (8)$$

These equations describe the motion of the point particles under the influence of gravity while accreting mass and momentum from the surrounding gas.

The Poisson equation is solved by multilevel elliptic solvers via the multigrid method. The potential ϕ is given by the Poisson equation

$$\nabla^2 \phi = 4\pi G \left[\rho + \sum_i M_i \delta(\mathbf{x} - \mathbf{x}_i) \right], \quad (9)$$

and the gas pressure P is given by

$$P = \frac{\rho k_B T_g}{\mu_p} = (\gamma - 1) \rho \left(e - \frac{1}{2} v^2 \right), \quad (10)$$

where T_g is the gas temperature, μ_p is the mean particle mass, and γ is the ratio of specific heats in the gas. We adopt $\mu_p = 2.33 m_H$, which is appropriate for standard cosmic abundances of a gas of molecular hydrogen and helium.

We use the sink particle implementation described in Krumholz et al. (2004) to replace cells which become too dense to resolve. Sink particle creation and AMR grid refinement are based on the Truelove criterion (Truelove et al. 1997) which defines the maximum density that can be well resolved in a grid code as

$$\rho < \rho_j = \frac{N_j^2 \pi c_s^2}{G (\Delta x^l)^2}, \quad (11)$$

where N_j is the Jeans number, here set to 0.125 for refinement, and 0.25 for sink creation, and Δx^l is the cell size on level l . When a cell violates the Jeans criterion, the local region is refined to the next highest grid level. If the violation occurs on the maximum level specified in the simulation, a sink particle is formed. Setting N_j to 0.125 is also consistent with the resolution criterion in Nelson (2006). Sink particles within four cells of each other are merged in order to suppress unphysical n -body interactions due to limited resolution. At low-resolution, unphysical sink particle formation and merging can cause rapid advection of sink particles inward onto the central star, generating spurious accretion. Moreover, because an isothermal, rotating gas filament will collapse infinitely to a line (Truelove et al. 1997; Inutsuka & Miyama 1992), an entire spiral arm can fragment and be merged into a single sink particle. To alleviate this problem, we implement a small barotropic switch in the gas equation of state such that

$$\gamma = 1.0001, \quad \rho < \rho_{J^s}/4, \quad (12)$$

$$\gamma = 1.28, \quad \rho_{J^s}/4 < \rho < \rho_{J^s}, \quad (13)$$

where the J^s subscript indicates the Jeans' criterion used for sink formation. With this prescription, gas is almost exactly isothermal until fragmentation is imminent, at which point it stiffens somewhat. This modest stiffening helps turn linear filaments into resolved spheres just prior to collapse and provides separation between newborn sink particles. The primary effect of this stiffening is to increase the resolution of the most unstable wavelength in a given simulation, at the expense of some dynamical range. We describe the influence of this stiffening on our results in Section 6.1, where we conduct some experiments in which it is turned off.

As described via Equations (3)–(6), sink particles both accrete from and interact with the gas and each other via gravity. Accretion rates are computed using a modified Bondi–Hoyle formula which prevents gas which is not gravitationally bound to the particles from accreting. See Krumholz et al. (2004) and Offner et al. (2008) for a detailed study of the effects of sink particle parameters. Note that we also use a secondary, spatial criterion for AMR refinement based on an analytic prediction for the disk size as a function of time (see Section 3.3).

3.2. Initial Conditions

We initialize each run with an isothermal sphere:

$$\rho(r) = \frac{A c_{s,\text{core}}^2}{4\pi G r^2}. \quad (14)$$

There is a small amount of rotational motion in our initial conditions, but no radial motion. A core with this profile is out of virial balance when $A > 2$ and accretes at a rate

$$\dot{M} = \frac{c_{s,\text{core}}^3}{G} \times \begin{cases} 0.975, & (A = 2) \\ (2A)^{3/2}/\pi & (A \gg 2) \end{cases}. \quad (15)$$

The value for $A = 2$ represents the Shu (1977) inside-out collapse solution, whereas the limit $A \gg 2$ is derived assuming pressureless collapse of each mass shell. It is possible to predict \dot{M} analytically (Shu 1977), but in practice we initialize our simulations with a range of values $A > 2$ and measure \dot{M} just outside the disk. Because our equation of state is isothermal up to densities well above the typical disk density ($c_{s,d} = c_{s,\text{core}}$), $MG/c_{s,\text{core}}^3$ is equivalent to our parameter ξ .

In order to set the value of our rotational parameter Γ and hold it fixed, we initialize our cores with a constant, subsonic rotational velocity:

$$v_{\text{rot}} = \varpi \Omega = 2Ac_s \left(\frac{\Gamma}{\xi} \right)^{1/3}, \quad (16)$$

where ϖ is the cylindrical radius. We arbitrarily choose a constant velocity rather than rigid rotation on spheres in order to concentrate accretion near the outer disk radii. Our definition of Γ in terms of the mean value of j_{in} rather than its maximum value is intended to reduce the sensitivity of our results to the choice of rotational profile.

Given these initial conditions, our parameters ξ and Γ remain constant throughout the simulation, while the collapsed mass and disk radius (as determined by the Keplerian circularization radius of the infalling material) increase linearly with time. We define a resolution parameter,

$$\lambda = \frac{R_{k,\text{in}}}{dx_{\text{min}}}, \quad (17)$$

to quantify the influence of numerics on our results. Because we hold the minimum grid spacing dx_{min} constant, λ increases $\propto t$ as the simulation progresses.

By artificially controlling the infall parameters of our disks and then watching them evolve in resolution, we gain insight into the physical behavior of accretion with certain values of ξ and Γ , as captured in a numerical simulation with a given dynamical range (λ). Our initial conditions are necessarily ideal, allowing us to perform controlled experiments. That we use a “core model” at all is purely for numerical convenience. Realistic star-forming cores will undoubtedly look very different with turbulence, and time varying accretion of mass and angular momentum, but before addressing more complicated scenarios we must establish the predictive value of our parameters.

3.3. Domain and Resolution

Due to the dimensionless nature of these experiments, we do not use physical units to analyze our runs. The base computational grid is 128^3 cells, and for standard runs we use nine levels of refinement, with a factor of 2 increase in resolution per level: this gives an effective resolution of $65,536^3$. More relevant to our results, however, is the resolution with which our disks are resolved: $\lambda \lesssim 10^2$. To compare this to relevant scales in star formation, this is equivalent to sub-AU resolution in disks of ~ 50 – 100 AU.

The initial core has a diameter equal to one half of the full grid on the base level. The gravity solver obeys periodic boundary conditions on the largest scale; as the disk is 2.5–3 orders of magnitude smaller than the grid boundaries, disk dynamics are unaffected by this choice. The initial radius of the current infall is $(\pi\Gamma)^{-2/3} R_{k,\text{in}}$ (from Equations (2), (14), and (15)); although this is much larger than the disk itself, it is still ~ 15 – 40 times smaller than the initial core and ~ 30 – 80 times smaller than the

base grid. Tidal distortions of the infall are therefore very small, although they may be the dominant seeds for the GI. We return to this issue in Section 6.2, where we compare two runs in which only the tidal effects should be different.

In addition to the density criterion for grid refinement described in Section 3, we also refine spatially to ensure that the entire disk is resolved at the highest grid level. We use ξ and Γ to predict the outer disk radius (see Section 4), and refine to the highest resolution within 1.5 times this radius horizontally, and within 0.4 times this radius vertically. We find that we accurately capture the vertical and radial extent of the disk with this prescription, and the density criterion ensures that any matter at disk densities extending beyond these radii will automatically be refined.

3.4. Dynamical Self-similarity

Because our goal is to conduct a parameter study isolating the effects of our parameters ξ and Γ , we hold each fixed during a single run. At a given resolution λ , we expect the simulation to produce consistent results regarding the behavior of the accretion disk, the role of GI, and the fragmentation of our idealized disks into binary or multiple stars. Since λ increases linearly in time, each simulation serves as a resolution study in which numerical effects diminish in importance as the run progresses. Because GI is an intrinsically unsteady phenomenon, a disk should fluctuate around its mean values even when all three of Γ , ξ , and λ are fixed. Because of this, and because λ changes over the run, we expect our runs to be self-similar, but only in a limited, statistical sense.

Moreover, whereas many physical systems are captured perfectly in the limit of infinite resolution ($\lambda \rightarrow \infty$), this is not true of isothermal, gravitational gas dynamics, in which the minimum mass and spacing of fragments both scale as λ^{-1} (Inutsuka & Miyama 1992). For this reason, we quote the resolution λ whenever reporting on the state of the disk-star system.

We note that there exists a minimum scale in real accretion disks as well, namely the opacity-limited minimum fragment mass (Rees 1976). The finite dynamical range of our numerical simulations is therefore analogous to a phenomenon of nature, albeit for entirely different reasons.

4. DISK PROPERTIES IN TERMS OF THE ACCRETION PARAMETERS

To assess the physical importance of ξ and Γ , it is useful to consider the case of a single star and its accretion disk. Because many ξ , Γ pairs lead to fragmentation, this assumption is only self-consistent within a subregion of our parameter space; nevertheless, it helps to guide our interpretation of the numerical results. In order to associate results from our parameters with those of previous studies, we also derive expressions for disk averaged quantities such as Q and the disk-to-system mass ratio, μ as a function of ξ and Γ .

The combination

$$\left(\frac{\Gamma}{\xi} \right)^{1/3} = \frac{\langle j \rangle_{\text{in}} c_{s,d}}{GM_{*d}} = \frac{c_{s,d}}{v_{k,\text{in}}} \quad (18)$$

is particularly useful, since it provides an estimate for the disk’s aspect ratio (the scale height compared to the circularization radius). Being independent of \dot{M} , it is more a property of the disk than of the accretion flow.

The other important dimensionless quantity whose mean value depends primarily on ξ and Γ (and slowly on resolution) is the disk-to-system mass ratio

$$\mu = \frac{M_d}{M_{*d}}. \quad (19)$$

When the disk is the sole repository of angular momentum, the specific angular momentum stored in the disk is related to the infalling angular momentum via

$$j_d = \left(\frac{J_{\text{in}}}{\langle j \rangle_{\text{in}} M_{*d}} \right) \frac{\langle j \rangle_{\text{in}}}{\mu}, \quad (20)$$

where J_{in} is the total angular momentum accreted, so that $J_{\text{in}} / (\langle j \rangle_{\text{in}} M_{*d}) = 1 / (l_j + 1)$ in an accretion scenario where $\langle j \rangle_{\text{in}} \propto M_{*d}^{l_j}$. In our simulations $l_j = 1$, so $j_d = \langle j \rangle_{\text{in}} / (2\mu)$. Given the relation between j_d and $\langle j \rangle_{\text{in}}$, we can define

$$\begin{aligned} R_d &= [(l_j + 1)\mu]^{-2} R_{k, \text{in}}, \\ \Omega_d &= [(l_j + 1)\mu]^3 \Omega_{k, \text{in}} \end{aligned} \quad (21)$$

which relate the disk's characteristic quantities (*not* the location of its outer edge) to conditions at the current circularization radius $R_{k, \text{in}} = \langle j \rangle_{\text{in}}^2 / (GM_{*d})$. Such “characteristic” quantities are valuable for describing properties of the disk as a whole, rather than at single location, with an effective mass weighting. If we further suppose that the disk's column density varies with radius as $\Sigma(r) \propto r^{-k_\Sigma}$ (we expect $k_\Sigma \simeq 3/2$ for a constant Q , isothermal disk), we may define its characteristic column density $\Sigma_d = (1 - k_\Sigma/2)M_d / (\pi R_d^2)$:

$$\Sigma_d \simeq f_\Sigma \frac{G^2 M_{*d}^3}{\langle j \rangle_{\text{in}}^4} \mu^5 \quad (22)$$

where $f_\Sigma = (1 - k_\Sigma/2)(1 + l_j)^4 / \pi$. Using Equations (18) and (21)–(22), we can rewrite the Toomre stability parameter Q (ignoring the difference between Ω and the epicyclic frequency, κ , for simplicity):

$$Q = \frac{c_s \kappa}{\pi G \Sigma} \rightarrow \frac{c_s \Omega_d}{\pi G \Sigma_d} \quad (23)$$

$$\begin{aligned} Q_d &\simeq \frac{f_Q^{-1}}{\mu^2} \frac{c_{s,d} \langle j \rangle_{\text{in}}}{GM_{*d}} \\ &= \left(\frac{\Gamma}{\xi} \right)^{1/3} \frac{f_Q^{-1}}{\mu^2}, \end{aligned} \quad (24)$$

where $f_Q = (1 - k_\Sigma/2)(1 + l_j)$. To the extent that we expect $Q_d \sim 1$ in any disk with strong GI, this suggests $\mu \sim (\Gamma/\xi)^{1/6} (1 - k_\Sigma/2)^{-1/2} (1 + l_j)^{-1/2}$; and because we expect that μ has an upper limit of around 0.5 (see Section 5 and discussion in KMK08 and Shu et al. 1990), we see there is an upper limit to ξ/Γ above which the system is likely to become binary or multiple. This is not surprising, as μ is proportional to the scale height when Q is constant; Equation (24) simply accounts self-consistently for the fact that μ also affects R_d .

To go any further with analytical arguments, we must introduce a Shakura & Sunyaev (1973) α viscosity parameterization, in which steady accretion occurs at a rate

$$\dot{M}_* = \frac{3\alpha}{Q_d} \frac{c_{s,d}^3}{G}. \quad (25)$$

Using the definition of ξ

$$\xi \simeq \frac{3\alpha}{Q_d} \frac{1}{1 - \mu}. \quad (26)$$

Insofar as $Q \sim 1$ when the GI is active, the effective value of α induced by a strong GI is directly proportional to ξ . We have made the simplifying assumption that accretion through the disk is roughly constant, although the factor of $(1 - \mu)$ accounts for the difference between the infall rate and the rate at which the disk processes material onto the star.

The magnitude of Γ has important implications for disk evolution. As discussed previously by KMK08, Γ (called \mathfrak{R}_{in} there) affects μ through the relation

$$\begin{aligned} \frac{\dot{\mu}}{\mu \Omega_{k, \text{in}}} &= \Gamma \left(\frac{1}{\mu} - 1 \right) - \frac{\dot{M}_*}{M_d \Omega_{k, \text{in}}}, \\ &\simeq \Gamma \left(\frac{1}{\mu} - 1 \right) - 3 \left(1 - \frac{k_\Sigma}{2} \right) (1 + l_j) \alpha \mu \left(\frac{\Gamma}{\xi} \right)^{2/3}, \end{aligned} \quad (27)$$

where the second line uses disk-averaged quantities to construct a mean accretion rate from Equation (25). Our runs approach a statistical steady state, $\dot{\mu} \simeq 0$ (although the dimensional quantity M_d continues to increase). We expect μ to saturate at the value for which the two terms on the right-hand side of Equation (27) are equal,

$$\mu \rightarrow (B^2 + 2B)^{1/2} - B, \text{ where } B = \frac{\Gamma^{1/3} \xi^{2/3}}{3(2 - k_\Sigma)(1 + l_j)\alpha}. \quad (28)$$

Here B is the linear coefficient for the quadratic in Equation (27). The disk mass fraction μ increases with B , so both Γ and ξ have a positive effect on μ , whereas α tends to suppress the disk mass.

The scaling of disk properties with ξ is in accord with intuitive expectations. An increase in ξ corresponds to an increase in accretion rate at fixed disk sound speed, and as a result the equilibrium disk mass rises. Similarly, an increase in α corresponds to an increase in the rate at which the disk can transport angular momentum and mass at a fixed rate of mass and angular momentum inflow, allowing the disk to drain and reducing its relative mass.

Less intuitive, however, is the fact that Equations (24) and (28) predict that rotation has a *stabilizing* effect on massive disk systems, in the sense that Q_d increases with Γ so long as $\mu > 0$. This can be seen by noting that $d \ln \mu / d \ln B = (1 - \mu) / (2 - \mu)$. Note that when B is small and $\mu \simeq \sqrt{2B}$, Equation (23) implies $Q_d \simeq 3\alpha/\xi$ in accordance with Equation (25). Thus for small values of μ , we recover the dependence of Q solely on ξ , in accord with Gammie (2001). As μ grows and saturates, Γ becomes more important in setting Q . We discuss the stabilizing influence of Γ in Section 5.3.

Because the effective value of α induced by the GI is a function of disk parameters, we cannot say more without invoking a model for $\alpha(\Gamma, \xi)$ or $\alpha(Q, \mu)$ as in KMK08. We use the above relations to guide our interpretation of our simulation results, specifically the dependence of disk parameters such as μ , Q_d , α , and the fragmentation boundary, on ξ and Γ .

5. RESULTS

Each of our runs produces either a disk surrounding a single star, or binary or multiple star system formed via disk

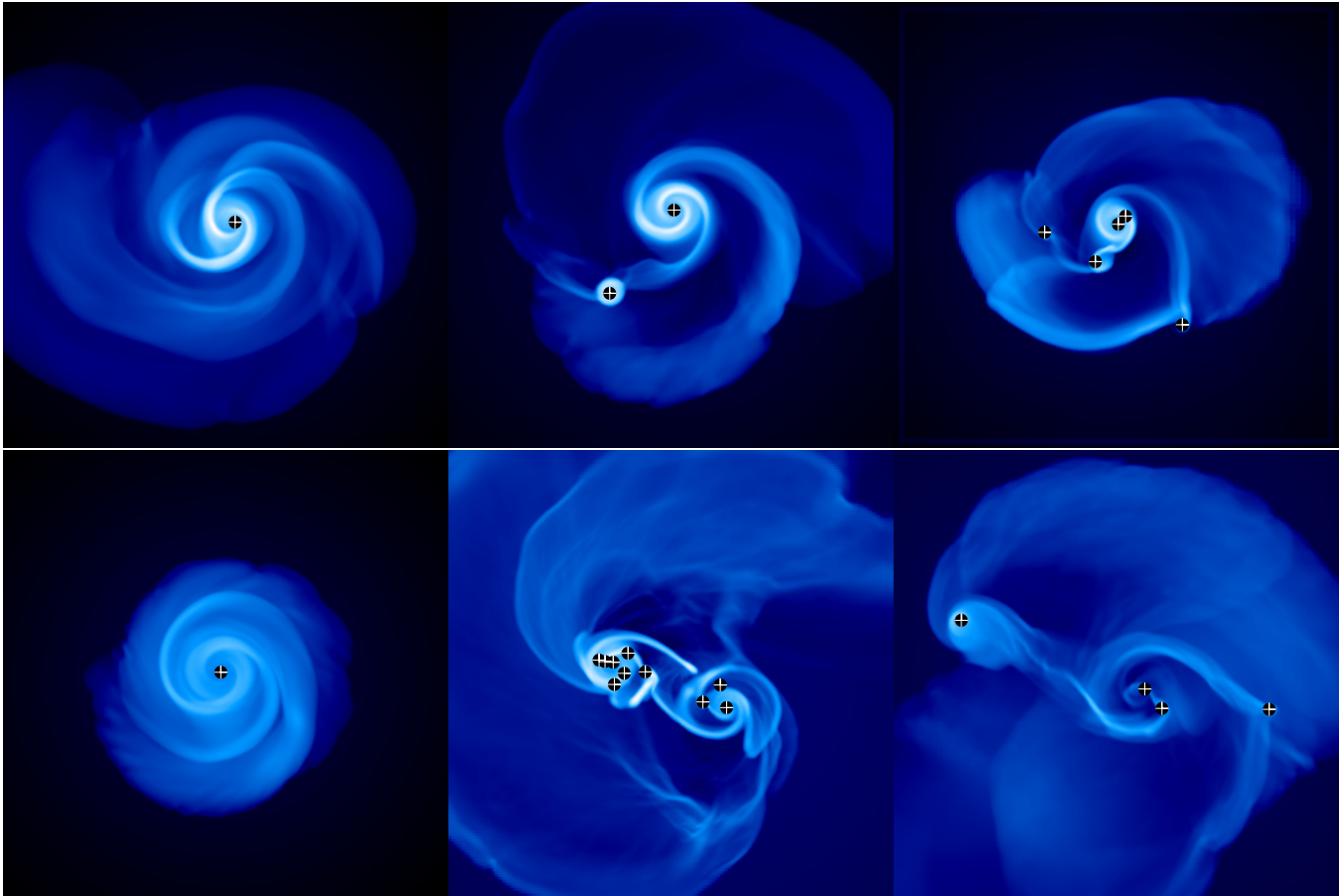


Figure 1. Two examples of single, binary, and multiple systems. The resolution across each panel is 328×328 grid cells. The single runs are $\xi = 2.9$, $\Gamma = 0.018$ (top), $\xi = 1.6$, $\Gamma = 0.009$ (bottom). The binaries are $\xi = 4.2$, $\Gamma = 0.014$ (top), $\xi = 23.4$, $\Gamma = 0.008$, (bottom). The multiples are $\xi = 3.0$, $\Gamma = 0.016$ (top), $\xi = 2.4$, $\Gamma = 0.01$ (bottom). Black circles with plus signs indicate the locations of sink particles. These correspond to runs 5, 1, 9, 16, 7, and 4, respectively. (A color version of this figure is available in the online journal.)

fragmentation; Figure 1 depicts examples of each outcome. We use these three possible morphologies to organize our description of the experiments. We explore the properties of each type of disk below as well as examine the conditions at the time of fragmentation.

The division between single and fragmenting disks in ξ and Γ is relatively clear from our results, as shown in Figure 2. Several trends are easily identified. First, there is a critical ξ beyond which disks fragment independent of the value of Γ . Below this critical ξ value, there is a weak stabilizing effect of increasing Γ . As ξ increases, disks transition from singles into multiples, and finally into binaries. We discuss the distinction between binaries and multiples in Section 5.4. This stabilizing effect of Γ is predicted by Equation (23), although it is somewhat counter intuitive. We discuss in Section 5.3 that the stabilization is often masked by thermal effects in real collapsing systems.

In Table 1, we list properties of the final state for all of our runs, their final multiplicity (S, B, or M for single, binary, or multiple, respectively), and the disk-to-star(s) mass ratio μ_f measured at the time at which we stop each experiment, as well as the maximum resolution λ_n . Note that the disk extends somewhat beyond $R_{k,in}$: therefore, the disk as a whole is somewhat better resolved than the value of λ_n would suggest. For the disks which fragment, we also list the values of μ_f , λ_f , and Q just before fragmentation occurs.

In Table 2, we describe those disks which do not fragment: we list the analytic estimate for the characteristic value of Toomre's

Q , Q_d , the measured minimum of Q_{2D} (Equation (29)), the radial power law k_Σ which characterizes $\Sigma(r)$ for a range of radii extending from the accretion zone of the inner sink particle to the circularization radius $R_{k,in}$, the final disk resolution, λ_n , and the characteristic disk radius, R_d (Equation (21)).

5.1. The Fragmentation Boundary and Q

It is difficult to measure a single value of Q to characterize a disk strongly perturbed by GI, so we consider two estimates: a two-dimensional measurement Q_{2D} , and a one-dimensional measure $Q_{av}(r)$ based on azimuthally averaged quantities.

$$Q_{2D}(r, \phi) = \frac{c_s \kappa}{\pi G \Sigma}, \quad (29)$$

$$Q_{av}(r) = \frac{\bar{c}_s(r) \bar{\kappa}(r)}{\pi G \bar{\Sigma}(r)}, \quad (30)$$

where bars represent azimuthal averages, and κ is calculated directly from the gravitational potential of the disk+stars. As Figure 3 shows, the two-dimensional estimate shows a great deal of structure which is not captured by the azimuthal average, let alone by Q_d . Moreover, while the minimum of the averaged quantity is close to 2, the two-dimensional quantity drops to $Q \sim 0.3$. We find that the best predictor of fragmentation is the minimum of a smoothed version of the two-dimensional quantity (smoothed over a local Jeans length to exclude meaningless

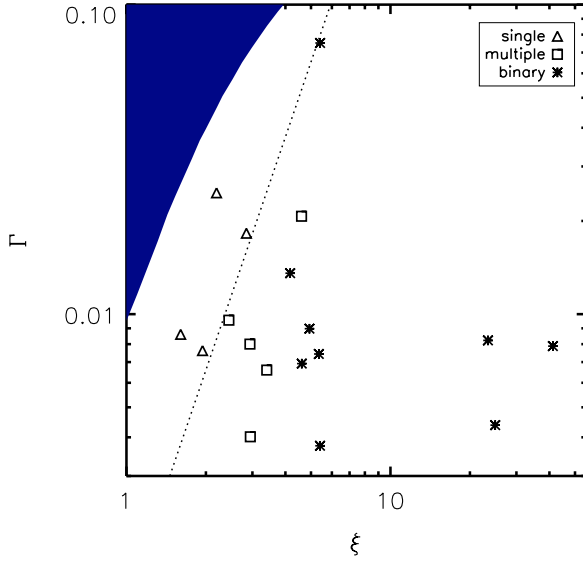


Figure 2. Distribution of runs in ξ - Γ parameter space. The single stars are confined to the low ξ region of parameters space, although increasing Γ has a small stabilizing effect near the transition around $\xi = 2$ due to the increasing ability of the disk to store mass at higher values of Γ . The dotted line shows the division between single and fragmenting disks: $\Gamma = \xi^{2.5}/850$. As ξ increases disks fragment to form multiple systems. At even higher values of ξ disks fragment to make binaries. We discuss the distinction between different types of multiples in Section 5.4. The shaded region of parameter space shows where isothermal cores no longer collapse due to the extra support from rotation.

(A color version of this figure is available in the online journal.)

Table 1

Each Run is Labeled by ξ , Γ , Multiplicity Outcome, the Final Value of the Disk-to-star(s) Mass Ratio, μ , and the Final Resolution, λ_n

| Run | ξ | $10^2\Gamma$ | N_* | μ_f | λ_f | Q_{2D} | μ | λ_n |
|-----|-------|--------------|-------|---------|-------------|----------|-------|-------------|
| 1 | 1.6 | 0.9 | S | ... | ... | ... | 0.49 | 99 |
| 2 | 1.9 | 0.8 | S | ... | ... | ... | 0.40 | 88 |
| 3 | 2.2 | 2.5 | S | ... | ... | ... | 0.56 | 82 |
| 4 | 2.4 | 1.0 | M | 0.43 | 77 | 0.69 | 0.16 | 98 |
| 5 | 2.9 | 1.8 | S | ... | ... | ... | 0.53 | 86 |
| 6 | 2.9 | 0.8 | M | 0.40 | 51 | 0.72 | 0.14 | 78 |
| 7 | 3.0 | 0.4 | M | 0.33 | 50 | 0.48 | 0.11 | 77 |
| 8 | 3.4 | 0.7 | M | 0.40 | 66 | 0.37 | 0.16 | 70 |
| 9 | 4.2 | 1.4 | B | 0.51 | 56 | 0.19 | 0.33 | 72 |
| 10 | 4.6 | 2.1 | M | 0.54 | 71 | 0.42 | 0.23 | 123 |
| 11 | 4.6 | 0.7 | B | 0.35 | 28 | 0.52 | 0.12 | 52 |
| 12 | 4.9 | 0.9 | B | 0.37 | 26 | 0.74 | 0.19 | 59 |
| 13 | 5.4 | 0.4 | B | 0.38 | 38 | 0.33 | 0.19 | 64 |
| 14 | 5.4 | 0.7 | B | 0.31 | 49 | 0.85 | 0.21 | 62 |
| 15 | 5.4 | 7.5 | B | 0.72 | 99 | 0.20 | 0.59 | 129 |
| 16* | 23.4 | 0.8 | B | 0.25 | 5 | 0.83 | 0.10 | 84 |
| 17* | 24.9 | 0.4 | B | 0.15 | 3 | 0.59 | 0.11 | 61 |
| 18* | 41.2 | 0.8 | B | 0.13 | 5 | 1.33 | 0.10 | 58 |

Notes. Values of Γ are quoted in units of 10^{-2} . For fragmenting runs the disk resolution λ_f , Q_{2D} (Equation (29)) and μ_f at the time of fragmentation are listed as well. S runs are single objects with no physical fragmentation. B's are binaries which form two distinct objects each with a disk, and M are those with three or more stars which survive for many orbits. * indicates runs which are not sufficiently well resolved at the time of fragmentation to make meaningful measures of μ_f and Q .

fluctuations), although Q_d shows a similar trend. We use this smoothed minimum quantity in Table 1, and compare it to the analytic estimate Q_d in Table 2 for non-fragmenting disks.

The critical values of Q at which fragmentation sets in depend on the exact method used for calculation (e.g., Q_{av} or Q_{2D}). The

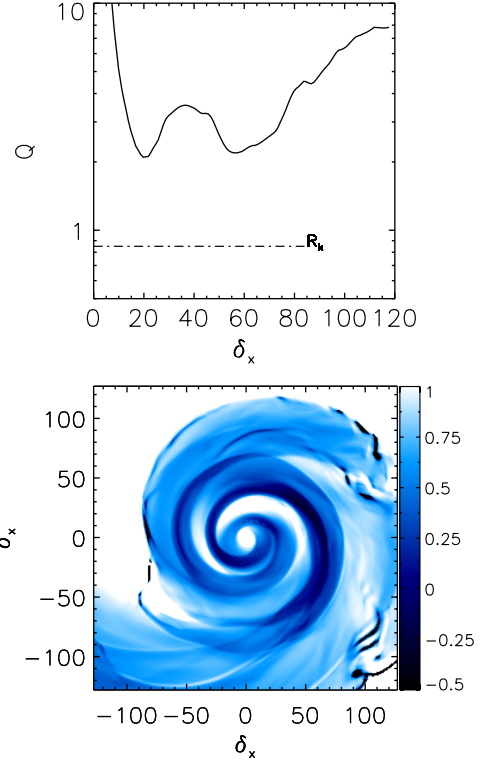


Figure 3. Top: Q_{av} in a disk with $\xi = 2.9$, $\Gamma = 0.018$. The current disk radius, $R_{k,in}$ is shown as well. Bottom: $\log(Q_{2D})$ (Equation (29)) in the same disk. While the azimuthally averaged quantity changes only moderately over the extent of the disk, the full two-dimensional quantity varies widely at a given radius. Q is calculated using κ derived from the gravitational potential, which generates the artifacts observed at the edges of the disk. Here and in all figures, we use δ_x to signify the resolution.

(A color version of this figure is available in the online journal.)

Table 2

Non-fragmenting Runs (Numbers as from Table 1)

| Run | ξ | $10^2\Gamma$ | μ | Q_d | Q_{2D} | k_Σ | λ_n | R_d |
|-----|-------|--------------|-------|-------|----------|------------|-------------|-------|
| 1 | 1.6 | 0.9 | 0.49 | 1.6 | 0.96 | 1.5 | 99 | 103 |
| 2 | 1.9 | 0.8 | 0.40 | 1.5 | 1.10 | 1.3 | 88 | 138 |
| 3 | 2.2 | 2.5 | 0.56 | 3.7 | 0.83 | 1.8 | 82 | 65 |
| 5 | 2.9 | 1.8 | 0.53 | 2.2 | 0.56 | 1.7 | 86 | 77 |

Notes. We list values for the characteristic predicted value of Toomre's Q , Q_d (Equation (23)), as well as the measured disk minimum, Q_{2D} Equation (29). We also list the slope of the surface density profile, k_Σ averaged over several disk orbits, the final resolutions, and R_d at the end of the run (Equation (21)).

canonical $Q = 1$ boundary only indicates the instability of axisymmetric perturbations in razor-thin disks (Toomre 1964). As discussed by numerous authors, the instability criterion is somewhat different for thick disks (Goldreich & Lynden-Bell 1965; Laughlin et al. 1997, 1998), and for the growth of higher order azimuthal modes (Adams et al. 1989; Shu et al. 1990; Laughlin & Korchagin 1996).

Because our disks are thick, the fragmentation boundary cannot be drawn in Q -space alone. We use Q_{2D} and μ in Figure 4 to demarcate the fragmentation boundary. Labeled curves illustrate that the critical Q for fragmentation depends on the disk scale height (Equation (18)). At a given value of Q , a disk with a larger value of μ will have a larger aspect ratio, and will therefore be more stable. Recall from Equation (18) that the disk aspect ratio is proportional to $(\xi/\Gamma)^{1/3}$.

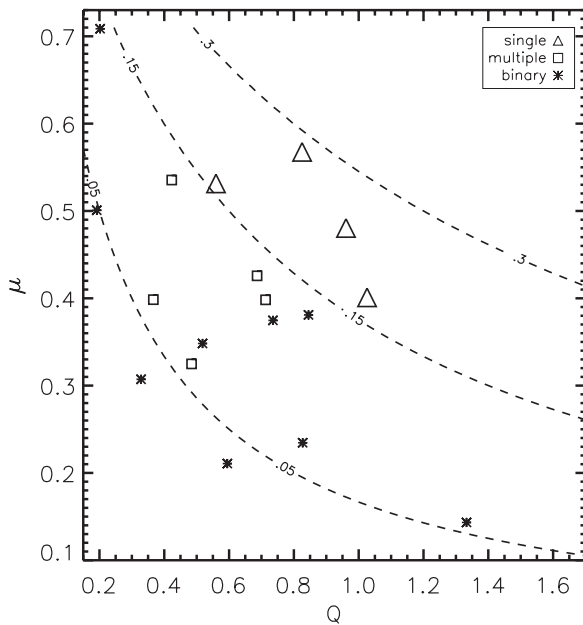


Figure 4. Steady-state and pre-fragmentation values of Q and μ for single stars and fragmenting disks, respectively. We use the minimum of Q_{2D} as described in Section 5.1. Symbols indicate the morphological outcome. Note that the non-fragmenting disks (large triangles) have the highest value of μ for a given Q . Contours show the predicted scale height as a function of Q and μ . It is clear that the single disks lie at systematically higher scale heights. We have assumed $k_{\Sigma} = 3/2$ in calculating scale height contours as a function of Q and μ .

This trend is consistent with the results of Goldreich & Lynden-Bell (1965) for thick disks; because the column of material is spread out over a larger distance, H , its self-gravity is somewhat diluted. The fact that two parameters are necessary to describe fragmentation is also apparent in Figure 2, where the boundary between single and multiple systems is a diagonal line through the parameter space.

5.2. Properties of Non-fragmenting Disks

We find that the disks show some evidence of a broken power-law structure: an inner region, characterized by k_{Σ} , where disk material is being accreted inward, and an outer region characterized by a steep, variable power law due to the outward spread of low-density, high angular momentum material. The inner disks are characterized by slopes between $k_{\Sigma} = 1$ –2. Clustering around $k_{\Sigma} = 3/2$ is expected, as this is the steady-state slope for a constant Q , isothermal disk. Our measurements of $Q(r)$ (Equation (29)) show fluctuating, but roughly constant value over the disk radius. Note that the slope of the inner disk region tends to increase with Γ . Figure 5 shows normalized radial profiles for the non-fragmenting disks. Profiles are averaged over approximately three outer-disk orbital periods. The flattening at small radii is due to the increasing numerical viscosity in this region (Section 6.2).

We find an upper mass limit of $\mu \sim 0.55$, for single stars, which means that disks do not grow more massive than their central star. A maximum disk mass has been predicted by Shu et al. (1990) as a consequence of the SLING mechanism. Such an upper limit is expected as eccentric gravitational instabilities in massive disks shift the center of mass of the system away from the central object. Indeed, we observe this wobble in binary forming runs. The subsequent orbital motion of the primary object acts as an indirect potential exciting strong $m = 1$ mode perturbations which can induce binary formation (Shu

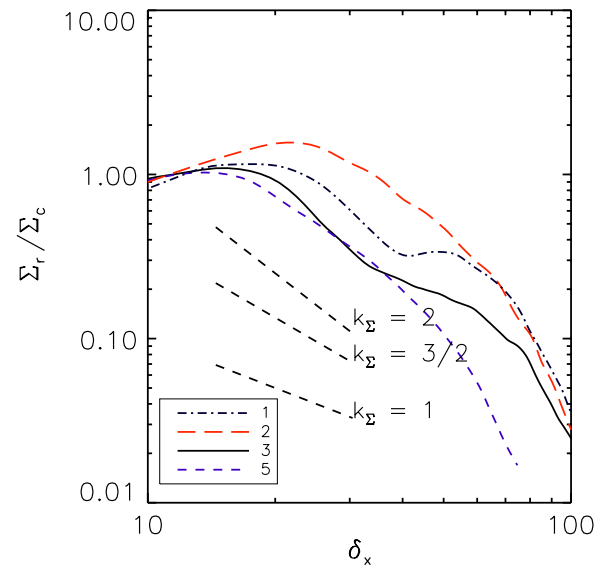


Figure 5. Normalized density profiles for the non-fragmenting disks. Profiles are azimuthal averages of surface densities over the final ~ 3 disk orbital periods. We find that while the inner regions are reasonably approximated by power-law slopes, the slope steepens toward the disk edge. For comparison, slopes of $k_{\Sigma} = 1, 1.5,$ and 2 are plotted as well. Runs are labeled according to their values in Table 1.

(A color version of this figure is available in the online journal.)

et al. 1990). Although our maximum value is higher than their prediction, the discrepancy may be related to the sharpness of their disk edge.

Using the analytic expressions above, we can also derive an expression for an effective Shakura–Sunyaev α . In this regime of parameter space, ξ and Γ are always such that $B \ll 1$ (assuming α does not stray far from unity). We therefore expect that $\mu \propto \Gamma^{1/6} \xi^{1/3} \alpha^{-1/2}$. Using this relation we can find a functional form of $\alpha(\xi, \Gamma)$. We find that

$$\mu \approx 2\Gamma^{1/3}, \quad (31)$$

with some scatter for both single disks and fragmenting disks just prior to fragmentation. We can use this fit to infer a scaling relation for α using Equation (28) in the limit $\mu \simeq \sqrt{2B}$:

$$\alpha_d \approx \frac{1}{18(2 - k_{\Sigma})^2(1 + l_j)^2} \frac{\xi^{2/3}}{\Gamma^{1/3}}. \quad (32)$$

The scaling is consistent with our expectation that driving the disk with a higher ξ causes it to process material more rapidly, while increasing Γ decreases the efficiency with which the disk accretes. Equation (32) predicts disk averaged values of α for single star disks between ~ 0.3 and 0.8 . These values are consistent with the observed accretion rates, and with numerically calculated torques (Section 5.5).

5.3. The Fragmentation Boundary

We find that the division between fragmenting and non-fragmenting disks can be characterized by a minimum value of Γ at which disks of a given ξ are stable. In Figure 2, we have plotted this empirically derived boundary as $\Gamma = \xi^{2.5}/850$. Although the fragmentation boundary may be influenced by disk resolution, our analytic predictions suggest that the moderate Γ dependence is physical. This result is consistent with the findings of Tohline (1981) and Tsuribe & Inutsuka (1999a) who

find cloud fragmentation below a critical value of $\alpha_{\text{therm}}\beta_{\text{rot}}$. For the cores which describe our initial conditions, $\alpha_{\text{therm}} = 3(\xi\pi)^{-2/3}$, while $\beta_{\text{rot}} = (\Gamma\pi)^{2/3}/4$. Although the mechanism for fragmentation is not identical (here fragmentation occurs after the central object has formed, in contrast to Tsuribe & Inutsuka 1999b), the $\alpha_{\text{therm}}\beta_{\text{rot}}$ criterion is equivalent to a restriction on $(H/R)^2$.

In disks with realistic temperature gradients, the stabilizing influence of rotation is overwhelmed by the fact that larger disks are typically colder, and have shorter cooling times relative to their orbital period, and therefore are more prone to fragmentation. In this case, more rotation does correspond to more fragmentation, as often observed (Walch et al. 2009). However, in our models we can distinguish between the effects of temperature and disk size (angular momentum). In the absence of a temperature gradient, a larger disk will be more stable because it can store more mass at lower column densities. In addition, Γ increases the disk aspect ratio, H/R , which also lowers the critical Q threshold for fragmentation.

5.4. The Formation of Binaries and Multiples

As shown by Figure 2, a large swath of our parameter space is characterized by binary and multiple formation. Are these equal mass binaries? Low mass stellar companions? Or maybe even massive planets? In our idealized self-similar picture it is difficult to tell. In an actively accreting multiple system, as long as the mass reservoir has angular momentum such that the circularization radius of the infalling material is comparable to the separation between objects, the smaller object, which is further from the center of mass, will accrete due to the torque imbalance (Bate & Bonnell 1997; Bonnell & Bate 1994b). Similarly, in thick, gravitationally unstable disks, the isolation mass approaches the stellar mass:

$$M_{\text{iso}} = 4\pi f_H r_H r_d \Sigma \approx \frac{f_H}{3.5} \left(\frac{10H}{R} \right)^{3/2} Q^{-3/2} M_*. \quad (33)$$

Here, $r_H = (M_s/3M_*)^{1/3}$ is the Hill radius, M_s and M_* are the masses of the secondary and primary, and the numerical factor f_H represents how many Hill radii an object can feed from in the disk—numerical simulations suggest $f_H \sim 3.5$ (Lissauer 1987; Rafikov 2002). Therefore, the evolution of these objects in our models is clear: they tend to equalize in mass. The binary separation will also grow if any of the infalling angular momentum is transferred to the orbits as opposed to the circumstellar disks. These trends are borne out in our experiments: binary mass ratios asymptote to values of 0.8–0.9 and separations to $\sim 60\%$ of $R_{k,\text{in}}$.

In a realistic model for star formation, the parameters that characterize a single run in this paper will represent only one phase in the life of a newborn system. The trajectory through ξ – Γ space which the systems take following binary formation will strongly influence the outcome in terms of separation and mass ratio.

5.4.1. Hierarchical Multiples and Resolution Dependence

Disks which are at the low ξ end of the binary forming regime tend to form binaries at later times, and therefore at higher disk resolution. Because of the numerical algorithm which forces sink particles within a gravitational softening length of each other to merge, at lower resolution many of these particles merge, leaving only two distinct objects behind. At higher

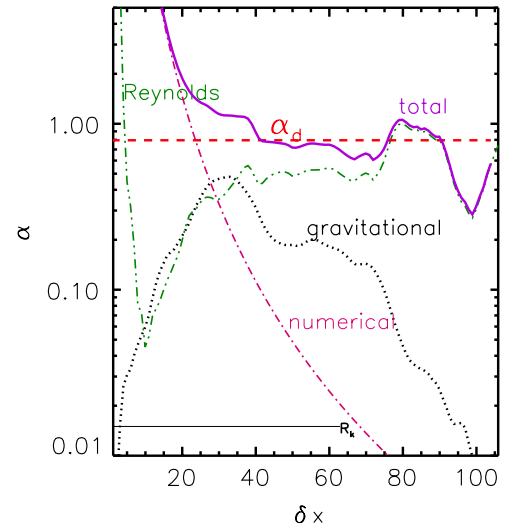


Figure 6. Azimuthal averages of different components of torque expressed as an effective α (Equation (35)) for run 8. The straight line, α_d (Equation (32)) is plotted for comparison. The agreement between the analytic value of α_d and the combined contribution from the other components is best near the expected disk radius $R_{k,\text{in}}$.

(A color version of this figure is available in the online journal.)

resolution, while some of the particles ultimately merge, we find that three or four objects typically survive this process. We cannot distinguish between merging and the formation of very tight binaries. In addition to merging, small mass fragments are occasionally ejected from the system entirely. This appears to be a stochastic process, though we have not done sufficient runs to confirm this conclusion.

5.5. Gravitational Torques and Effective α

We verify that the accretion observed in our disks is generated by physical torques by computing the net torque in the disk. It is convenient to analyze the torques in terms of the stress tensor, $T_{R\phi}$, which is made up of two components: large-scale gravitational torques and Reynolds stresses. Following Lodato & Rice (2005) we define

$$T_{R\phi} = \int \frac{g_R g_\phi}{4\pi G} dz + \Sigma \delta \mathbf{v}_R \delta \mathbf{v}_\phi, \quad (34)$$

where $\delta \mathbf{v} = \mathbf{v} - \bar{\mathbf{v}}$. In practice, we set $\delta \mathbf{v}_R = \mathbf{v}_R$, while $\delta \mathbf{v}_\phi$ is calculated with respect to the azimuthal average of the rotational velocity at each radius. In reality there is an extra viscous term attributable to numerical diffusion. We discuss the importance of this term in Section 6.2.

The first term in Equation (34) represents torques due to large-scale density fluctuations in spiral arms, while the second is due to Reynolds stresses from deviations in the velocity field from a Keplerian (or at least radial) velocity profile. To facilitate comparison with analytic models, the torques can be represented as an effective α where

$$T_{R\phi} = \left| \frac{d \ln \Omega}{d \ln R} \right| \alpha \Sigma c_s^2. \quad (35)$$

We can compare these torques to the characteristic disk α_d in Equation (32) at a snapshot in time. Figure 6 compares α_d to the azimuthal average of the physical torques for one of our runs. We also show the expected contribution from numerical diffusion (see Section 6.2). The accretion expected from these

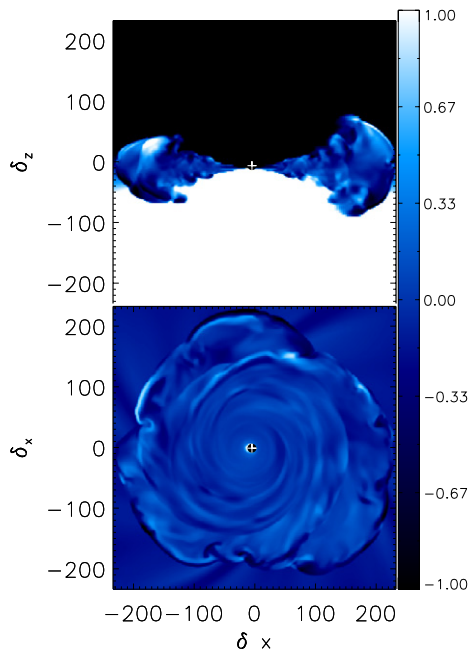


Figure 7. Cuts along the vertical axis and disk midplane of the vertical velocity, normalized to the disk sound speed. Clearly most of the vertical motions in the disk are transonic, although at the edges of the disk the velocities exceed $\mathcal{M} \sim 1$.

(A color version of this figure is available in the online journal.)

three components is consistent with the time averaged total accretion rate onto the star. Due to the short-term variability of the accretion rate, the two do not match up exactly. It is interesting to note the radial dependence of the Reynolds stress term, which in the inner region decays rapidly, before rising again, due to the presence of spiral arms. In both the azimuthal average and the two-dimensional distribution we see that at small radii numerical diffusion dominates, whereas at large radii deviations in the azimuthal velocity which generate Reynolds stresses are spatially correlated with the spiral arms.

5.6. Vertical Structure

When the disks reach sufficient resolution, we can resolve the vertical motions and structure of the disk. We defer a detailed analysis of the vertical structures to a later paper, but discuss several general trends here. Depending on the run parameters, the disk scale height is ultimately resolved by 10–25 grid cells. We observe only moderate transonic motions in the vertical direction of order $\mathcal{M} \sim 1$ –2. Figure 7 shows two slices of the z -component of the velocity field for a single system, one through the X – Z plane, and the other through the disk midplane. Although there is significant substructure, the motions are mostly transonic. Figure 8 illustrates the range of disk aspect ratios as a function of ξ and Γ .

6. CAVEATS AND NUMERICAL EFFECTS

6.1. Isothermal Equation of State

Many simulations have shown the dramatic effects that thermodynamics have on disk behavior (Boss et al. 2000; Gammie 2001; Rice et al. 2005; Lodato & Rice 2005; Boley et al. 2006; Krumholz et al. 2007; Offner et al. 2009). Since we are concerned with fragmentation, we must be aware of the potential dependences of the fragmentation boundary on cooling physics. Starting with Gammie (2001), there has been much

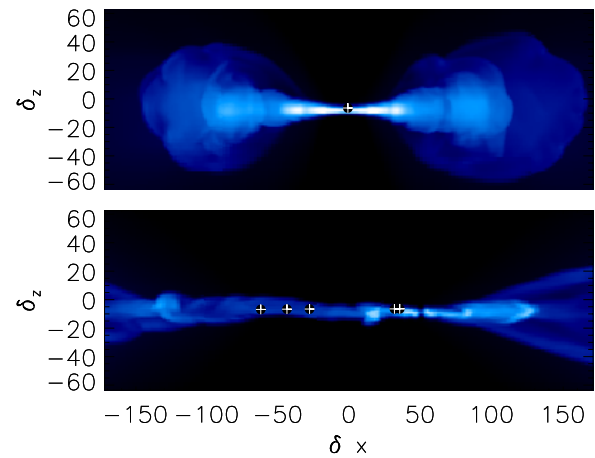


Figure 8. Density slices showing vertical structure in a single and binary disk. The top plot is a single star with $\xi = 1.6$, $\Gamma = 0.009$, while the bottom is a fragmenting binary system with $\xi = 24.3$, $\Gamma = 0.008$. Equation (18) predicts disk aspect ratios of 0.18 and 0.07, respectively. The extended material in the binary system is generated by a combination of large-scale circumbinary torques and the infalling material. Color scale is logarithmic. The box sizes are scaled to $1.5R_{k,in}$ in the plane of the disk.

(A color version of this figure is available in the online journal.)

discussion of the “cooling time constraint” that states that a disk with $Q \sim 1$ will only fragment if the cooling time is short. While this is a valuable analysis tool for predicting the evolution of a system from a snapshot and for quantifying the feedback from gravito-turbulence, for most of the protostellar disks that we are modeling, the cooling time at the location of fragmentation is short because irradiation is the dominant source of heating (D’Alessio et al. 1997; Matzner & Levin 2005; Krumholz et al. 2007; Kratter et al. 2008).

Passively heated disks behave more like isothermal disks than barotropic disks, because the energy generation due to viscous dissipation is small compared to the energy density due to radiation. Consequently, feedback from accretion in the midplane does not alter the disk temperature significantly. Numerical simulations such as Krumholz et al. (2007) find that strongly irradiated disks appear locally isothermal. In fact, the morphological outcome is similar to those of Krumholz et al. (2007) with comparable values of ξ .

Another possible concern is the lack of a radial temperature gradient, independent of the equation of state. Both passively and actively (through viscous dissipation) heated disks will be warmer at small radii. In these experiments, we find spiral arms persist in regions where the average value of Q is well above that at which instability is presumed to set in, with local values exceeding this by an order of magnitude. It seems plausible that due to the global nature of the low- m spiral modes, angular momentum transport may still occur in regions one would assume stable against GI. As discussed by Adams et al. (1989), $m = 1$ modes can have appreciable growth rates for $Q > 1$ even when the evanescent region covers as much as 70% of the disk radius. At small radii where the disk becomes stable, another mechanism for transport must take over. Alternatively, material from the outer, unstable portion of the disk will likely accumulate until the critical surface density for GI is reached.

In order to test the effects of the gas stiffening we introduced to avoid unphysical merging of our sink particles (see Section 3.1), we have conducted several purely isothermal experiments in which it is turned off. The removal of the barotropic switch artificially enhances accretion at early times due to sink particles

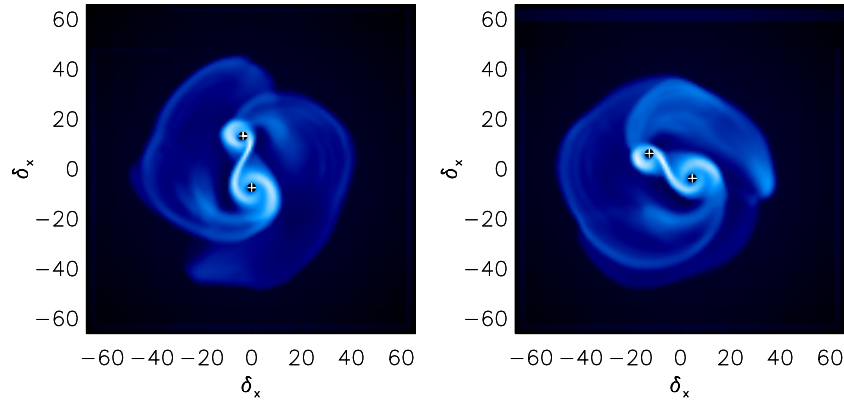


Figure 9. Left: snapshot of the standard resolution of run 16 shortly after binary formation. Right: the same run at double the resolution. Because of the self-similar infall prescription, we show the runs at the same numerical resolution, as time and resolution are interchangeable. In this case, the high-resolution run has taken twice the elapsed “time” to reach this state. The two runs are morphologically similar and share expected disk properties.

(A color version of this figure is available in the online journal.)

formed via numerical fragmentation merging with the central star. Removing the barotropic switch is equivalent to increasing the resolution of the fragmentation process, but decreasing the resolution of the scale of fragmentation relative to λ , the disk resolution. Using a barotropic switch allows the disk to reach a higher λ before fragmentation sets in for a given set of parameters.

6.2. Resolution

We have shown in Section 5.5 that the observed accretion is consistent with the combined gravitational torques and Reynold stresses, and that these are dominant over that expected purely from numerical diffusion. Because of the self-similar infall, convergence to a steady state within a given run is a good indicator that numerics are not determining our result; in effect, every run is a resolution study. That we observe a range of behavior at the same resolution but different input parameters also imply that numerical effects are sub-dominant. We consider our disks to be resolved when they reach radii such that $R_{k,in}/\Delta x \geq 30$. The effective numerical diffusivity, which we plot in Figure 6, has been estimated by Krumholz et al. (2004) for ORION. Specifically they find that

$$\alpha_{\text{num}} \approx 78 \frac{r_B}{\Delta x} \left(\frac{r}{\Delta x} \right)^{-3.85}, \quad (36)$$

where

$$r_B = \frac{GM_*}{c_s^2} \quad (37)$$

is the standard Bondi radius.

For our typical star and disk parameters, this implies numerical α 's of order 0.1–0.3 at the minimum radius at which we are resolved, so at most 1/3 of our effective α could be attributed to numerical effects at low resolution. See discussions by Offner et al. (2008); Krumholz et al. (2007, 2004) for a detailed analysis of disk resolution requirements. At our resolution of 50–100 radial cells across the disk, the dominant effect of numerical diffusion is likely a suppression of fragmentation (Shetty & Ostriker 2006; Nelson 2006). Because the isothermal spiral arms can become very narrow prior to fragmentation, numerical diffusion across an arm may smear out some overdensities faster than they collapse. Therefore, the conclusions regarding the fragmentation boundary are likely conservative.

We demonstrate morphology convergence in one of our binary runs. We rerun run 16 (as labeled in Table 1) at double the

resolution (128^3 with 10 levels of refinement as opposed to 9). Increasing the physical resolution also decreases the code time step proportionally so that the ratio of the timestep to orbital period as a function of λ should be preserved. In fact, there is little that can be different between the runs at two resolutions at the same effective λ .

The two runs have the same morphology and characteristic disks properties as a function of λ , as expected. We show in Figure 9 snapshots of the standard and high resolution runs. The standard resolution run (left) is at twice the elapsed “time” of the high resolution one (right), and so the same numerical resolution, λ . We confirm that the mass accretion rate is consistent between the two runs: at the snapshots shown the mass ratio of the lower resolution run is 0.46, while the higher resolution run is 0.48. To the extent that numerical artifacts are seeding instabilities, we expect some stochasticity in the details of the fragmentation between any two runs. Although the effect is small, it is also possible that since the physical size of the disk (and the radius from which material is currently accreting) relative to the box size is larger at the same value of λ for the low resolution run, the large-scale quadrupole potential from the image masses is stronger in the low resolution case.

7. COMPARISON TO PREVIOUS STUDIES

The literature is replete with useful simulations of protostellar and protoplanetary disks at various stages of evolution, however most involve isolated disks, without infall at large radii (Laughlin & Bodenheimer 1994; Laughlin & Rozyczka 1996; Rice et al. 2005; Lodato & Rice 2005; Fromang & Nelson 2006; Shetty & Ostriker 2006; Boley et al. 2006; Lodato et al. 2007; Cai et al. 2008). These simulations include a wide range of physics, from magnetic fields to radiative transfer, but due to the lack of infalling matter, they neither develop disk profiles (surface density, temperature) self-consistently, nor do they enter the regime of interest in this work: rapid accretion in the embedded phase. For a review of many of the issues addressed by current GI disk simulations, see Durisen et al. (2007).

There are a few simulations of self-consistent growth and evolution (Vorobyov & Basu 2007, 2008). These are ideal for following the long-term evolution of more quiescent lower mass disks. However, because they are two dimensional, and lack a moving central potential, they cannot follow the evolution of non-axisymmetric modes which are driven by the displacement of the central star from the center of mass, nor can they

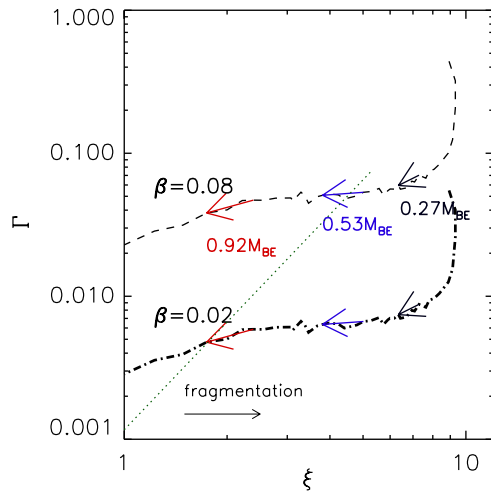


Figure 10. Trajectory of a Bonnor–Ebert sphere through ξ – Γ space. The two lines show values of $\beta = 0.02, 0.08$ as defined in Matsumoto & Hanawa (2003). Arrows indicate the direction of time evolution from $t/t_{\text{ff},0} = 0$ –5. $t_{\text{ff},0}$ is evaluated with respect to the central density, and arrows are labeled with the fraction of the total Bonnor–Ebert mass which has collapsed up to this point. The dotted line shows the fragmentation boundary from Figure 2.

(A color version of this figure is available in the online journal.)

accurately simulate the formation of multiple systems. Other authors have investigated the initial stage of core collapse onto disks (Tsuribe & Inutsuka 1999b; Banerjee & Pudritz 2007), however, these authors focus on the effects of magnetic fields and fragmentation of the core prior to disk formation, respectively. Tsuribe & Inutsuka (1999b) and Matsumoto & Hanawa (2003) have also investigated the collapse of cores into disks and binaries, though they do not investigate many disk properties (see Section 7.1 for detailed comparisons). Krumholz et al. (2007) and Krumholz et al. (2009) have conducted three-dimensional radiative transfer calculations, but due to computational cost can only investigate a small number of initial conditions.

In addition to numerical work, there are a range of semi-analytic models which follow the time evolution of accreting disks (Hueso & Guillot 2005; KMK08). KMK08 examined the evolution of embedded, massive disks in order to predict regimes in which gravitational instability, fragmentation of the disk, and binary formation were likely. They concluded that disks around stars greater than 1–2 M_{\odot} were likely subject to strong gravitational instability, and that a large fraction of O and B stars might be in disk-born binary systems.

7.1. The Evolution of the Accretion Parameters in the Isothermal Collapse of a Bonnor–Ebert Sphere

While self-similar scenarios are useful for numerical experiments, they do not accurately capture the complexities of star formation. In particular, in realistic cores, ξ and Γ evolve in time. Therefore, it is interesting to chart the evolution of a more realistic (though still idealized) core through our dimensionless parameter space. We consider the isothermal collapse of a Bonnor–Ebert sphere initially in solid-body rotation (Bonnor 1956). Such analysis allows us to compare our results with other numerical simulations that have considered global collapse and binary formation such as Matsumoto & Hanawa (2003) via the parameters laid out in Tsuribe & Inutsuka (1999a).

We use the collapse calculation of a 10% overdense, non-rotating Bonnor–Ebert sphere from Foster & Chevalier (1993), and impose angular momentum on each shell to emulate solid

body rotation. Figure 10 shows the trajectory of a rotating Bonnor–Ebert sphere through ξ – Γ parameter space as a function of time in units of the central initial freefall time $t/t_{\text{ff},0}$, for two different rotation rates corresponding to $\beta_{\text{rot}} = 0.02, 0.08$.

The early spike in ξ is due to the collapse of the inner flattened core. Similarly, the corresponding decline in Γ is a result of the mass enclosed increasing more rapidly than the infalling angular momentum. The long period of decreasing ξ and constant Γ arises from the balance between larger radii collapsing to contribute more angular momentum and the slow decline of the accretion rate. This trajectory may explain several features of the fragmentation seen in Matsumoto & Hanawa (2003). Although not accounted for in Figure 10, cores with high values of β have accretion rates suppressed at early times due to the excess rotational support, while those with low β collapse at the full rate seen in Foster & Chevalier (1993). In cores with small β , the high value of ξ may drive fragmentation while the disk is young. Alternatively, for modest values of β , Γ may be sufficiently low while ξ is declining that the disk mass surpasses the critical fragmentation threshold, and fragments via the so-called satellite formation mechanism. For very large values of β , a core which is only moderately unstable will oscillate and not collapse as seen in Matsumoto & Hanawa (2003) for $\beta > 0.3$.

8. DISCUSSION

We have examined the behavior of gravitationally unstable accretion disks using three-dimensional, AMR numerical experiments with the code ORION. We characterize each experiment as a function of two dimensionless parameters, ξ and Γ , which are dimensionless accretion rates comparing the infall rate to the disk sound speed and orbital period, respectively. We find that these two global variables can be used to predict disk behavior, morphological outcomes, and disk-to-star accretion rates and mass ratios. In this paper, we discuss the main effects of varying these parameters. Our main conclusions are as follows.

1. Disks can process material falling in at up to $\xi \sim 2$ –3 without fragmenting. Although increasing Γ stabilizes disks at fixed values of ξ those fed at $\xi > 3$ for many orbits tend to fragment into a multiple or binary system.
2. Disks can reach a statistical steady state where mass is processed through the disk at a fixed fraction of the accretion rate onto the disk. The discrepancy between these two rates, μ , scales with Γ ; disks with larger values of Γ can sustain larger maximum disk masses before becoming unstable. The highest disk mass reached in a non-fragmenting system is $\mu \approx 0.55$ or $M_* \sim M_d$.
3. Gravitational torques can easily produce effective accretion rates consistent with a time averaged $\alpha \approx 1$.
4. The minimum value of Q at which disks begin to fragment is roughly inversely proportional to the disk scale height. It is therefore important to consider not only Q but another dynamical parameter when predicting fragmentation, at least in disks which are not thin and dominated by axisymmetric modes.
5. The general disk morphology and multiplicity is consistent between isothermal runs and irradiated disks with similar effective values of ξ .

These conclusions are subject to the qualification that fragmentation occurs for lower values of ξ as the disk resolution increases, and so it is possible that the location of the fragmentation boundary will shift with increasing resolution (K. M. Kratter et al. 2010, in preparation). However, we expect

that our results are representative of real disks and other numerical simulations insofar as they have comparable dynamic range of the parameters relevant to fragmentation such as λ_J/λ .

The authors thank Chris McKee, Jonathan Dursi, Stella Offner, Andrew Cunningham, Norman Murray, and Yanqin Wu for insightful discussions and technical assistance, and an anonymous referee for helpful comments. K.M.K. was funded in part by an Ontario Graduate Scholarship. C.D.M. received support through an Ontario Early Research Award, and by NSERC Canada. M.R.K. received support for this work from an Alfred P. Sloan Fellowship, from NASA, as part of the Spitzer Theoretical Research Program, through a contract issued by the JPL, and from the National Science Foundation, through grant AST-0807739. R.I.K. received support for this work provided by the US Department of Energy at Lawrence Livermore National Laboratory under contract DE-AC52-07NA 27344; NASA through ATP grant NNX09AK31G and NSF through grant AST-908553. All computations were performed on the Canadian Institute for Theoretical Astrophysics Sunnyvale cluster, which is funded by the Canada Foundation for Innovation, the Ontario Innovation Trust, and the Ontario Research Fund. This research was supported in part by the National Science Foundation under grant no. PHY05-51164.

REFERENCES

- Adams, F. C., Ruden, S. P., & Shu, F. H. 1989, *ApJ*, **347**, 959
- Banerjee, R., & Pudritz, R. E. 2007, *ApJ*, **660**, 479
- Barnes, P. J., Yonekura, Y., Ryder, S. D., Hopkins, A. M., Miyamoto, Y., Furukawa, N., & Fukui, Y. 2008, arXiv:0812.1789
- Bate, M. R., & Bonnell, I. A. 1997, *MNRAS*, **285**, 33
- Beltrán, M. T., Cesaroni, R., Codella, C., Testi, L., Furuya, R. S., & Olmi, L. 2006, *Nature*, **443**, 427
- Bodenheimer, P., Tohline, J. E., & Black, D. C. 1980, *ApJ*, **242**, 209
- Boley, A. C., Mejía, A. C., Durisen, R. H., Cai, K., Pickett, M. K., & D'Alessio, P. 2006, *ApJ*, **651**, 517
- Bonnell, I. A., & Bate, M. R. 1994a, *MNRAS*, **269**, L45
- Bonnell, I. A., & Bate, M. R. 1994b, *MNRAS*, **271**, 999
- Bonnor, W. B. 1956, *MNRAS*, **116**, 351
- Boss, A. P., Fisher, R. T., Klein, R. I., & McKee, C. F. 2000, *ApJ*, **528**, 325
- Cai, K., Durisen, R. H., Boley, A. C., Pickett, M. K., & Mejía, A. C. 2008, *ApJ*, **673**, 1138
- D'Alessio, P., Calvet, N., & Hartmann, L. 1997, *ApJ*, **474**, 397
- Durisen, R. H., Boss, A. P., Mayer, L., Nelson, A. F., Quinn, T., & Rice, W. K. M. 2007, in *Protostars and Planets V*, ed. B. Reipurth, D. Jewitt, & K. Keil (Tucson, AZ: Univ. Arizona Press), 607
- Fisher, R. T. 2002, PhD thesis, Univ. California, Berkeley
- Foster, P. N., & Chevalier, R. A. 1993, *ApJ*, **416**, 303
- Fromang, S., & Nelson, R. P. 2006, *A&A*, **457**, 343
- Gammie, C. F. 2001, *ApJ*, **553**, 174
- Goldreich, P., & Lynden-Bell, D. 1965, *MNRAS*, **130**, 125
- Goodman, A. A., Benson, P. J., Fuller, G. A., & Myers, P. C. 1993, *ApJ*, **406**, 528
- Hueso, R., & Guillot, T. 2005, *A&A*, **442**, 703
- Inutsuka, S.-I., & Miyama, S. M. 1992, *ApJ*, **388**, 392
- Klein, R. I. 1999, *J. Comput. Appl. Math.*, **109**, 123
- Kratter, K. M., & Matzner, C. D. 2006, *MNRAS*, **373**, 1563
- Kratter, K. M., Matzner, C. D., & Krumholz, M. R. 2008, *ApJ*, **681**, 375
- Krumholz, M. R. 2006, *ApJ*, **641**, L45
- Krumholz, M. R., Klein, R. I., & McKee, C. F. 2007, *ApJ*, **656**, 959
- Krumholz, M. R., Klein, R. I., McKee, C. F., Offner, S. S. R., & Cunningham, A. J. 2009, *Science*, **323**, 754
- Krumholz, M. R., McKee, C. F., & Klein, R. I. 2004, *ApJ*, **611**, 399
- Larson, R. B. 1972, *MNRAS*, **156**, 437
- Laughlin, G., & Bodenheimer, P. 1994, *ApJ*, **436**, 335
- Laughlin, G., & Korchagin, V. 1996, *ApJ*, **460**, 855
- Laughlin, G., Korchagin, V., & Adams, F. C. 1997, *ApJ*, **477**, 410
- Laughlin, G., Korchagin, V., & Adams, F. C. 1998, *ApJ*, **504**, 945
- Laughlin, G., & Rozyczka, M. 1996, *ApJ*, **456**, 279
- Lin, D. N. C., & Pringle, J. E. 1987, *MNRAS*, **225**, 607
- Lissauer, J. J. 1987, *Icarus*, **69**, 249
- Lodato, G., Meru, F., Clarke, C. J., & Rice, W. K. M. 2007, *MNRAS*, **374**, 590
- Lodato, G., & Rice, W. K. M. 2005, *MNRAS*, **358**, 1489
- Matsumoto, T., & Hanawa, T. 2003, *ApJ*, **595**, 913
- Matzner, C. D., & Levin, Y. 2005, *ApJ*, **628**, 817
- Matzner, C. D., & McKee, C. F. 2000, *ApJ*, **545**, 364
- Miyama, S. M., Hayashi, C., & Narita, S. 1984, *ApJ*, **279**, 621
- Myers, P. C., & Fuller, G. A. 1992, *ApJ*, **396**, 631
- Nelson, A. F. 2006, *MNRAS*, **373**, 1039
- Offner, S. S. R., Klein, R. I., & McKee, C. F. 2008, *ApJ*, **686**, 1174
- Offner, S. S. R., Klein, R. I., McKee, C. F., & Krumholz, M. R. 2009, *ApJ*, **703**, 131
- Rafikov, R. R. 2002, *ApJ*, **572**, 566
- Rees, M. J. 1976, *MNRAS*, **176**, 483
- Rice, W. K. M., Lodato, G., & Armitage, P. J. 2005, *MNRAS*, **364**, L56
- Shakura, N. I., & Sunyaev, R. A. 1973, *A&A*, **24**, 337
- Shetty, R., & Ostriker, E. C. 2006, *ApJ*, **647**, 997
- Shu, F. H. 1977, *ApJ*, **214**, 488
- Shu, F. H., Tremaine, S., Adams, F. C., & Ruden, S. P. 1990, *ApJ*, **358**, 495
- Tohline, J. E. 1981, *ApJ*, **248**, 717
- Toomre, A. 1964, *ApJ*, **139**, 1217
- Truelove, J. K., Klein, R. I., McKee, C. F., Holliman, II, J. H., Howell, L. H., & Greenough, J. A. 1997, *ApJ*, **489**, L179
- Truelove, J. K., Klein, R. I., McKee, C. F., Holliman, II, J. H., Howell, L. H., Greenough, J. A., & Woods, D. T. 1998, *ApJ*, **495**, 821
- Tsuribe, T., & Inutsuka, S.-I. 1999a, *ApJ*, **526**, 307
- Tsuribe, T., & Inutsuka, S.-I. 1999b, *ApJ*, **523**, L155
- Vorobyov, E. I., & Basu, S. 2007, *MNRAS*, **381**, 1009
- Vorobyov, E. I., & Basu, S. 2008, *ApJ*, **676**, L139
- Walch, S., Burkert, A., Naab, T., & Gritschneider, M. 2009, *MNRAS*, **400**, 13
- Whitworth, A., Bate, M. R., Nordlund, A., Reipurth, B., & Zinnecker, H. 2007, in *Protostars and Planets V*, ed. B. Reipurth, D. Jewitt, & K. Keil (Tucson, AZ: Univ. Arizona Press), 459
- Williams, J. P., & Myers, P. C. 1999, *ApJ*, **511**, 208